Crystal structure and magnetic properties of complex oxides $Mg_{4-x}Ni_xNb_2O_9$, $0 \leqslant x \leqslant 4$

N.V. Tarakina[a,b,*], E.A. Nikulina[a], J. Hadermann[b], D.G. Kellerman[a], A.P. Tyutyunnik[a], I.F. Berger[a], V.G. Zubkov[a], G. Van Tendeloo[b]

[a]*Institute of Solid State Chemistry, Ural Branch of Russian Academy of Sciences, Ekaterinburg GSP-145, 620219 Ekaterinburg, Russian Federation*
[b]*EMAT, University of Antwerp, Groenenborgerlaan 171, Antwerp, Belgium*

Abstract

In the $Mg_{4-x}Ni_xNb_2O_9$ ($0 \leqslant x \leqslant 4$) system two ranges of solid solution have been found. One of the solid solutions has a corundum-related structure type (space group $P\bar{3}c1$); the second one adopts the II-$Ni_4Nb_2O_9$ structure type (space group $Pbcn$). The unit cell constants and atomic positions have been determined and refined using neutron powder diffraction data. Electron diffraction and high-resolution transmission electron microscopy (HRTEM) from $MgNi_3Nb_2O_9$ crystals identify the presence of planar defects and the intergrowth of several (structurally related) phases. The magnetic susceptibility of $Mg_3NiNb_2O_9$, measured in the temperature range $T = 2–300$ K, shows no indications of magnetic ordering at low temperatures, while for $MgNi_3Nb_2O_9$ there is a magnetic ordering at temperatures below 45.5 K.
© 2007 Elsevier Inc. All rights reserved.

Keywords: Magnesium niobium oxide; Neutron powder diffraction; Rietveld refinement; Crystal structure; Electron diffraction; HREM; Magnetic properties

1. Introduction

The rapid development of wireless communication technologies has pushed researchers to look for new dielectric materials, which will allow increasing selectivity and considerably reducing the size of the devices working at high frequencies. Such materials could be used as dielectric resonators, superconducting microwave filters and as substrates for integrated circuits. The latter consist of a substrate with a low value of dielectric losses and a superconducting film, usually $YBa_2Cu_3O_{7-x}$ [1]. As the substrate material often corundum (Al_2O_3) or complex aluminum oxides ($LaAlO_3$, Sr_2AlTaO_6, Sr_2AlNbO_6 and etc.) are used [2–4]. However, they have a number of disadvantages: Al_2O_3 chemically reacts with the superconducting film while $LaAlO_3$, Sr_2AlNbO_6 and Sr_2AlTaO_6 are sintered at temperatures $> 1600 \, ^\circ C$, too high for commercial use.

The microwave dielectric properties of corundum-related $Mg_4Nb_2O_9$ compare well with those of Al_2O_3 [5], moreover the diniobate does not react with the superconducting film and has a sintering temperature up to $1400 \, ^\circ C$. The influence of various substitutes on the sintering temperature and microwave properties of $Mg_4Nb_2O_9$ has also been investigated [6–10]. It was shown that in the $Mg_4Nb_2O_9$–$Ni_4Nb_2O_9$ system only solid solutions $Mg_{4-x}Ni_xNb_2O_9$ ($x = 0–2$) based on the $Mg_4Nb_2O_9$ structure type (space group $P\bar{3}c1$) could be formed; the $Q \, f$ values sharply decrease with increasing nickel content from 192,268 up to 28,440 GHz [10]. However, it has been shown in several works that the microwave properties strongly correlate not only with the chemical composition but also with changes in the structure and microstructure [11]. In this case, the microstructure of the $Mg_{4-x}Ni_xNb_2O_9$ ($x = 0–4$) solid solutions and the possibility of its formation on the base of the $Ni_4Nb_2O_9$ structure (space group $Pbcn$) [12] become

*Corresponding author. Institute of Solid State Chemistry, Ural Branch of Russian Academy of Sciences, Ekaterinburg GSP-145, 620219 Ekaterinburg, Russian Federation. Fax: +7 343 3744495.

E-mail address: tarakina@ihim.uran.ru (N.V. Tarakina).

interesting. On the other side, the substitution of Mg^{2+} by Ni^{2+} can also influence the magnetic properties of the concerned niobates, introducing the possibility of applying an external magnetic field as a driving force for modeling magnetic fields passing through the sample.

The main goal of this contribution is a detailed investigation of the solid solutions in the $Mg_4Nb_2O_9$–$Ni_4Nb_2O_9$ system. Further we want to establish any correlation between the crystal structure, microstructure and properties of the concerned compounds.

2. Experiment

Magnesium, nickel and niobium (V) oxides (99.9%) were used as starting materials. The initial materials were mixed according to the required cation ratio, grounded in an agate mortar with acetone, pressed into pellets and placed in a platinum crucible. Pellets were heated with a speed of 5 °C/min and annealed at a temperature of 1300 °C during 10–12 h followed by cooling 5 °C/min.

The samples for X-ray diffraction were thoroughly crushed in ethanol and placed with vaseline between two lavsan films. The X-ray powder diffraction (XRD) pattern was collected at room temperature on a Bragg-Brentano STADI-P (STOE, Germany) diffractometer equipped with a scintillation detector, using $CuK\alpha$ radiation in the 2θ range 2–120° with a step of 0.02°. Polycrystalline silicon ($a = 5.43075(5)$ Å) was used as external standard. The phase purity of the samples was checked by comparing their XRD with those in the PDF2 database (Powder diffraction file, ICDD, USA, release 2005). The neutron studies were performed at room temperature; the powder sample was placed in a vanadium container with a diameter of 6 mm and a wall thickness less than 0.1 mm. Neutron powder diffraction data were collected at room temperature using the 7A diffractometer at the IWW 2M reactor (Zarechny) in the 2θ range 2–120° with a step of 0.02°, $\lambda = 1.5323$ Å. The crystal structure has been refined with the GSAS program suite [13] using neutron powder diffraction data.

For the transmission electron microscopy (TEM) studies the samples were crushed in ethanol. A drop of this dispersion was put on a copper grid covered with a holey carbon film. The EDX analysis and electron diffraction (ED) patterns were obtained using a Philips CM20 operated at 200 kV, equipped with an Oxford INCA system. High-resolution TEM (HRTEM) observations were performed using a JEOL 4000 EX microscope, operated at 400 kV. Simulations of HREM images were made using the JEMS software.

Magnetic measurements were made on a SQUID-magnetometer MPMS-5XL (quantum design) in the temperature range $T = 2$–300 K and varying in the field up to 30 kOe.

3. Results

3.1. Synthesis and crystal structure

Two ranges of solid solution have been found in the system $Mg_4Nb_2O_9$–$Ni_4Nb_2O_9$. In the first range solid

solutions $Mg_{4-x}Ni_xNb_2O_9$ ($0 \leqslant x \leqslant 2.75$) with a structure based on the corundum-related phase $Mg_4Nb_2O_9$, space group $P\bar{3}c1$ ($Z = 2$) are formed. In the second range, a solid solution $Mg_{4-x}Ni_xNb_2O_9$ ($2.75 < x \leqslant 4$) with a structure based on the II-$Ni_4Nb_2O_9$ structure (space group. $Pbcn$; $Z = 4$) is formed. The changes of the unit cell parameters and volume with x are shown in Fig. 1. Since the solid state solutions of the first and the second range have different crystal symmetries, the hexagonal lattice has been transformed into an orthorhombic lattice in order to compare them: $a_{orth} = \sqrt{3}\, a_{trig}$, $c_{orth} = c_{trig}$. In both solid solutions, a smooth change of the unit cell parameters and volume with x has been observed. The deviation from a linear dependence in the case of $MgNi_3Nb_2O_9$ can be explained by its structural features.

Two samples $Mg_3NiNb_2O_9$ and $MgNi_3Nb_2O_9$ from the first and the second range, respectively, have been chosen for a detailed crystal structure investigation. An analysis of the XRD and ED data shows that $Mg_3NiNb_2O_9$ crystallizes in a trigonal unit cell with parameters: $a = 5.1484(1)$,
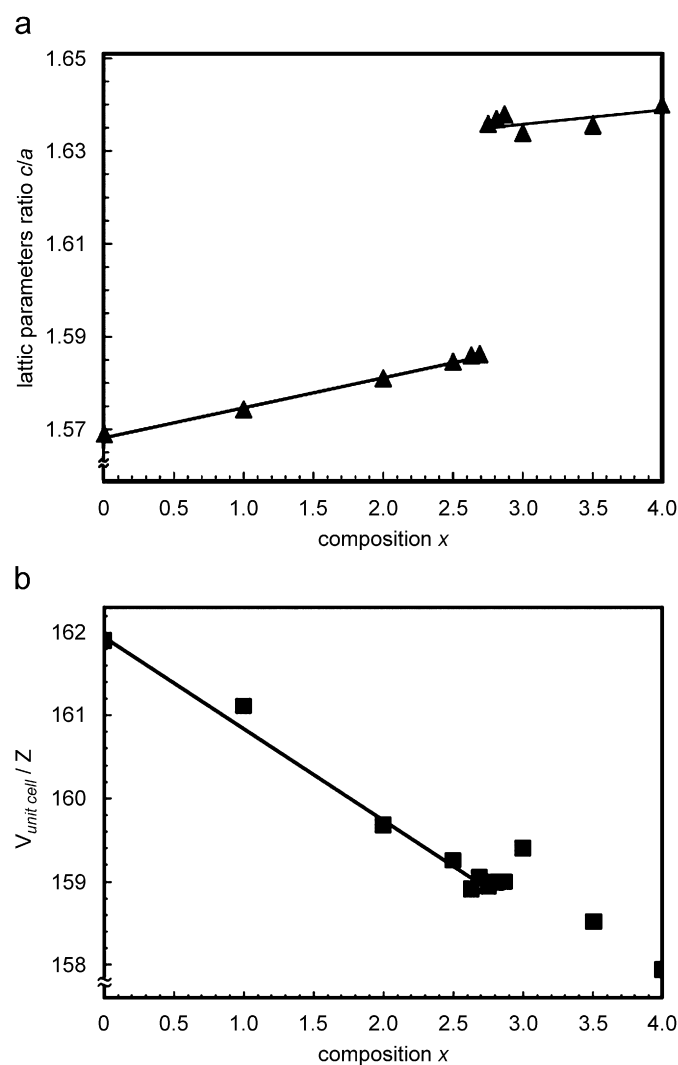

Fig. 1. (a) Ratio between c and a unit cell parameters and (b) unit cell volumes for solid solutions $Mg_{4-x}Ni_xNb_2O_9$ ($0 \leqslant x \leqslant 4$).

$c = 14.0363(3)$ Å. The reflection conditions ($00l$: $l = 2n$, h-hl: $l = 2n$) indicate a primitive lattice, with possible space groups: $P\bar{3}c1$, $P3c1$ ($Z = 2$). $MgNi_3Nb_2O_9$ crystallizes in an orthorhombic unit cell with parameters: $a = 8.7652(2)$, $b = 5.0893(1)$, $c = 14.3087(3)$ Å. The reflection conditions ($0kl$: $k = 2n$, $h0l$: $l = 2n$, $hk0$: $h + k = 2n$, $h00$: $h = 2n$, $0k0$: $k = 2n$, $00l$: $l = 2n$) point towards the $Pbcn$ ($Z = 4$) space group. Selected area diffraction patterns of $Mg_3NiNb_2O_9$ and $MgNi_3Nb_2O_9$ are shown in Figs. 2 and 3, respectively. The appearance of the forbidden reflections $0\,0\,l$ ($l=2n$) on the [100] pattern of $MgNi_3Nb_2O_9$ is due to double diffraction; this is seen by the fact that the reflections disappear when rotating the crystal away from the perfect orientation around this axis. It is also evident from their absence on the [010] ED pattern. The elemental content of the 10–15 crystallites for $Mg_3NiNb_2O_9$ and $MgNi_3Nb_2O_9$ compositions was investigated by EDX analysis performed inside the electron microscope. Obtained compositions

Fig. 2. Electron diffraction patterns of $Mg_3NiNb_2O_9$ along the main zone axes.

Fig. 3. Electron diffraction patterns of $MgNi_3Nb_2O_9$ along the main zone axes.

showed slight inhomogeneous cation distribution and are $Mg_{3.0(3)}Ni_{1.0(3)}Nb_{2.0(2)}$ and $Mg_{1.0(2)}Ni_{2.8(3)}Nb_{2.2(2)}$ for the $Mg_3NiNb_2O_9$ and $MgNi_3Nb_2O_9$, respectively. $Mg_4Nb_2O_9$ [14] and II-$Ni_4Nb_2O_9$ [15] were used as starting models for the crystal structure refinement of $Mg_3NiNb_2O_9$ and $MgNi_3Nb_2O_9$, respectively. The background was described with a shifted Chebyshev polynomial with 15 variables and the peak shape with a pseudo-Voigt function. In order to refine the site-occupation factors three different models have been proposed for solid solutions based on $Mg_4Nb_2O_9$ (or $Ni_4Nb_2O_9$):

(a) Niobium atoms occupy $4c$ ($8d$) position; magnesium and nickel atoms statistically occupy two $4d$ ($8d$) positions.
(b) Niobium atoms occupy $4c$ ($8d$) position; magnesium occupies $4d$ ($8d$) position, the other $4d$ ($8d$) position is shared by nickel and magnesium atoms with a ratio 0.5/0.5.
(c) All three positions are occupied statistically.

The best fit between experimental and theoretical data has been found for model (a).

For the case of $MgNiNb_2O_9$, a problem with describing the peak shape at $2\theta = 42.85°$, $62.93°$, $86.45°$ and $111.8°$ was found during the structure refinement. Including NiO as a second phase into the refinement gave a better correlation. The refinement converged with $wR_p = 3.62\%$, $R_p = 2.57\%$, $Dw_d = 0.575$, $R(F^2) = 3.05\%$, $\chi2 = 2.639$ and $wR_p = 2.41\%$, $R_p = 1.82\%$, $Dw_d = 0.931$, $R(F^2) = 1.64\%$, $\chi^2 = 2.92$ for $Mg_3NiNb_2O_9$ and $MgNi_3Nb_2O_9$, respectively. Details of the refinement, atomic coordinates and temperature factors can be found in Tables 1 and 2. The calculated, observed and difference patterns are shown in Fig. 4.

$Mg_3NiNb_2O_9$ and $MgNi_3Nb_2O_9$ represent corundum related structures, which can be described as layers of hexagonally close packed oxygen atoms with 2/3 of the octahedral sites occupied by metal atoms. In corundum-related compounds with more than one metal atom, the sequence and/or ordering of the cations along the c direction usually plays an important role. For $MgNi_3Nb_2O_9$ and $MgNi_3Nb_2O_9$, the sequence of cations is identical. It consists of layers containing Mg and Ni atoms, which alternate with two layers containing both Mg, Ni and Nb (Fig. 5). The difference lies in the way that the cations fill

Table 1
Atomic coordinates and isotropic thermal parameters for $Mg_3NiNb_2O_9$

Atom		x/a	y/b	z/c	$U_i/U_e \times 100$	Occupation
Mg1/Ni1	$4d$	0.6667	0.3333	0.8083(4)	0.27(23)	0.80/0.20
Mg2/Ni2	$4d$	0.6667	0.3333	0.5141(4)	0.95(22)	0.70/0.30
Nb	$4c$	0	0	0.3579(3)	0.63(11)	1
O1	$6f$	0.2902(9)	0	0.25	0.38(13)	1
O2	$12g$	0.9756(1)	0.6537(5)	0.4165(4)	0.98(8)	1

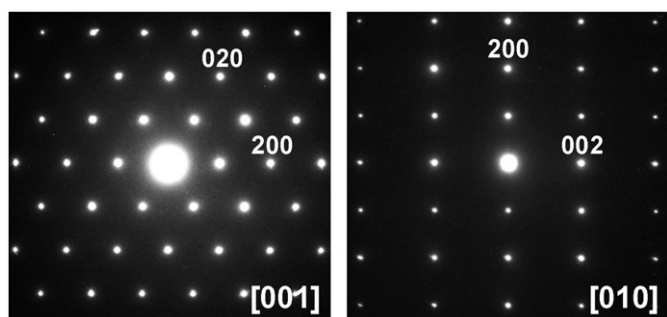$wR_p = 3.62\%$, $R_p = 2.57\%$, $Dw_d = 0.575$, $R(F^2) = 3.05\%$ and $\chi^2 = 2.639$.
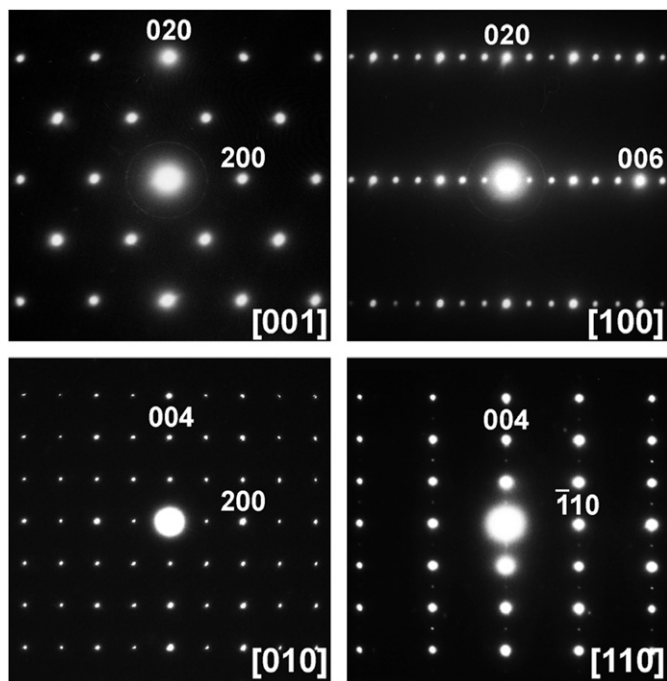
Table 2
Atomic coordinates and isotropic thermal parameters for $MgNi_3Nb_2O_9$

Atom		x/a	y/b	z/c	$U_i/U_e \times 100$	Occupation
Mg1/Ni1	8d	0.3366(4)	0.9959(10)	0.6884(2)	0.31(4)	0.27/0.73
Mg2/Ni2	8d	0.3357(5)	0.9944(15)	0.5067(2)	0.74(4)	0.23/0.77
Nb	8d	0.0252(3)	0.9985(14)	0.8556(2)	0.35(6)	1
O1	4c	0	0.7165(14)	0.25	0.17(20)	1
O2	8d	0.1679(7)	0.1686(9)	0.9272(4)	1.00(13)	1
O3	8d	0.1647(5)	0.1714(8)	0.5946(4)	0.46(10)	1
O4	8d	0.1508(5)	0.1462(13)	0.2507(3)	0.40(13)	1
O5	8d	0.5072(5)	0.1663(11)	0.9143(6)	0.17 (12)	1

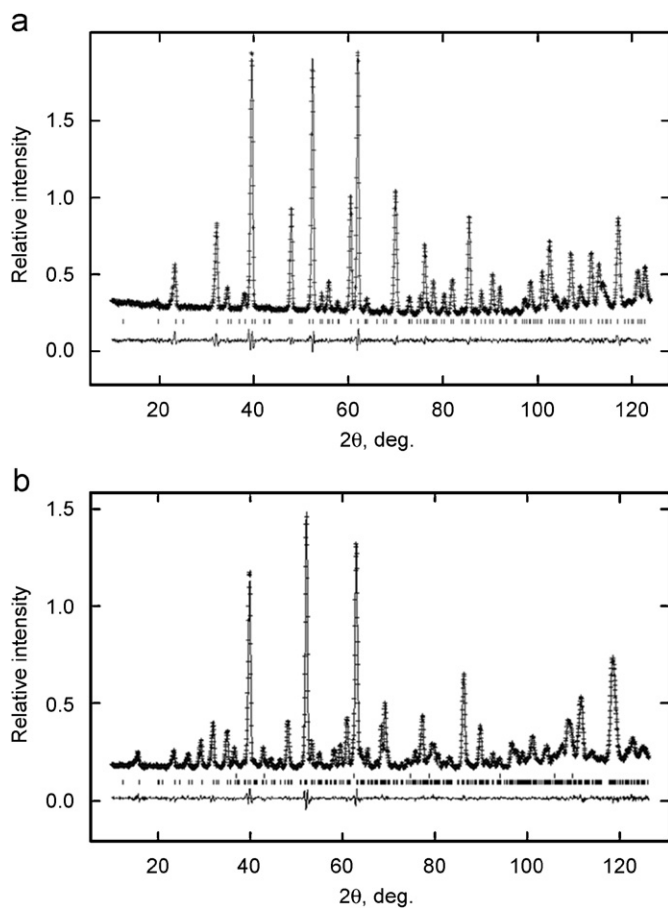$wR_p = 2.41\%$, $R_p = 1.82\%$, $Dw_d = 0.931$, $R(F^2) = 1.64\%$ and $\chi^2 = 2.92$.

Fig. 4. Observed (crosses), calculated (solid line) and difference (bottom) powder diffraction patterns of $Mg_3NiNb_2O_9$ (a) and $MgNi_3Nb_2O_9$ (b).

Fig. 5. Crystal structure of (a) $Mg_3NiNb_2O_9$, (b) $MgNi_3Nb_2O_9$. Red (dark grey)—$(Mg,Ni)O_6$; yellow (light grey)—NbO_6.

the octahedral sites in the hexagonally close packed oxygen layers. In the case of $Mg_3NiNb_2O_9$ each MO_6 octahedron is connected via edge-sharing to three other octahedra forming a honey-comb pattern (C). In the case of $MgNi_3Nb_2O_9$, the layers containing Mg and Ni have a honey-comb pattern as well (C), but in the Mg–Ni–Nb layers each NbO_6 octahedron is connected via edge-sharing to three octahedrons, whereas $(Mg,NiO)_6$ is connected via edge-sharing to five octahedrons, which leads to a chain pattern (S) (Fig. 6). Along the c direction such layers will stack as –(CCC)–(CCC)– for $Mg_3NiNb_2O_9$ and as

–(CSS)–(CSS)– for $MgNi_3Nb_2O_9$ (Fig. 5). This stacking has been confirmed by ED as well as by HRTEM imaging.

In some diffraction patterns of $MgNi_3Nb_2O_9$ though, lines of diffuse scattering along the c^* direction have been observed (Fig. 7). Moreover, sometimes clear maxima are observed in the patterns. To clear up the origin of these imperfections, HRTEM has been performed on crystals with and without diffuse scattering along c^*.

The presence of the chains in the $MgNi_3Nb_2O_9$ structure leads to a reduction of the crystal symmetry from trigonal (corundum-related compounds) to orthorhombic; therefore projections along [010] and [110] become nonequivalent. On the [010] HRTEM image of Fig. 8, taken at a focus value around −40 nm, the intense white reflections correspond to the tunnels in the structure; this is confirmed by the simulated images (inset Fig. 8). The sequence of blocks –(CSS)– with tunnels (white dots) can therefore be established along the b direction. In order to simplify the description, the –(CSS)– blocks will be labeled –X–, hereafter. The configuration in Fig. 8 can therefore be described as …XX…

Viewing the structure along [110], the same blocks, but rotated over 60° around the c axis, overlap and there is no longer a chain structure. On the corresponding HRTEM images no tunnels can be discerned anymore. We will label the rotated blocks –X′– (Fig. 9). The simulated images again confirm the structural interpretation.

In regions where the [110] ED patterns show extended diffuse scattering, planar defects or bands are observed.
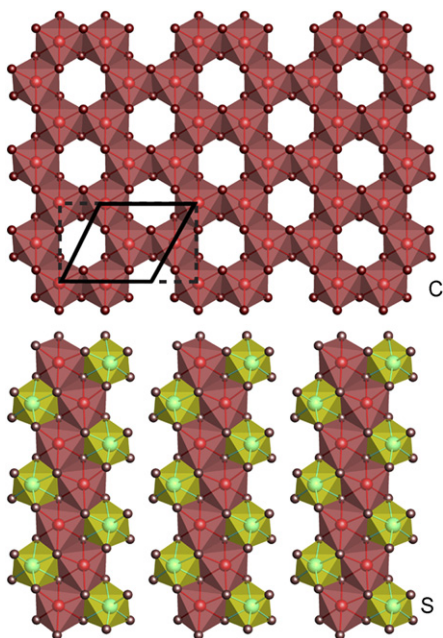
Fig. 6. Two types of corundum layers: C-honey-comb pattern, S-chains pattern. Red (light grey)—$(Mg,Ni)O_6$; yellow (dark grey)—NbO_6. Line—$Mg_3NiNb_2O_9$ unit cell, dotted line—$MgNi_3Nb_2O_9$.
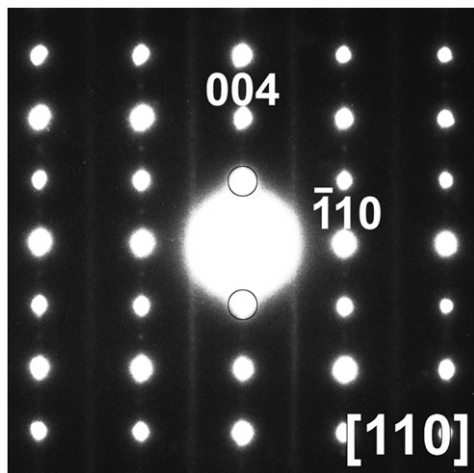

Fig. 7. Electron diffraction patterns of $MgNi_3Nb_2O_9$ along the [110] axis showing diffuse streaks.

Fig. 8. [010] HREM image of $MgNi_3Nb_2O_9$. The simulation for defocus of −40 nm, thickness of 4 nm is indicated by a white border.

Fig. 9. [110] HREM image of $MgNi_3Nb_2O_9$. The simulation for defocus of −37 nm, thickness of 5 nm is indicated by a white border.

They are all perpendicular to the c-axis, but randomly distributed. The width of the bands is varying though (Fig. 10a). On the corresponding HRTEM images and with the previous X and X′ code in mind, the different sequences can be analyzed. Clearly both X and X′ blocks are present along [110] (Fig. 10b). Since the hexagonally close packed oxygen layers have 6-fold symmetry, the tunnels in different layers can be formed in directions rotated over 60° relative to each other. Several stacking sequences of X and X′ blocks have been observed in HRTEM images of defect crystals. In Fig. 10b the sequence –X–X′–X′–X– appears on a pseudo-regular basis, forming locally a long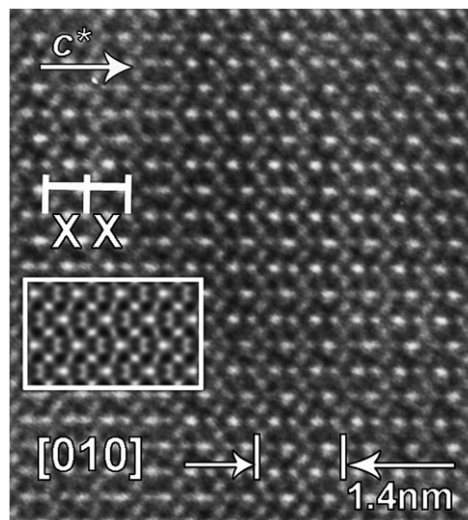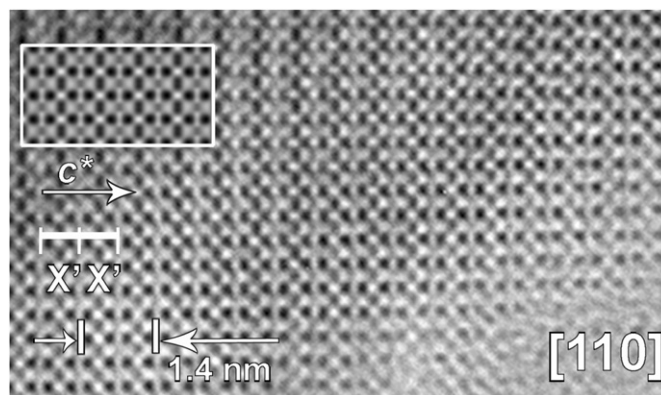 period superstructure. Apart from the rotation, also a translation can take place; this is also seen in Fig. 10b, where at the left, for sequence (1) all blocks lie on one row; i.e. no translation along the a-axis in hexagonal unit cell. For the sequence at the right (2), the blocks –X′–X– are shifted over half of the a-axis in the hexagonal unit cell. In some crystals, a regular sequence –X′–X–X′–X– occurs with blocks –X′–X– displaced every time over half of the a-axis in the hexagonal unit cell (Fig. 11). It is known from the literature that such sequence of layers produces the I-$Ni_4Nb_2O_9$ modification [12]; however, in the case of $MgNi_3Nb_2O_9$, it was not found as a bulk crystal, but rather as a defective structure.

This stacking regime and the flexibility of the structure to form them, allows us to propose the possibility of different ordering schemes between the X and X′ blocks. Based on these modifications of corundum related structures new materials could be prepared.
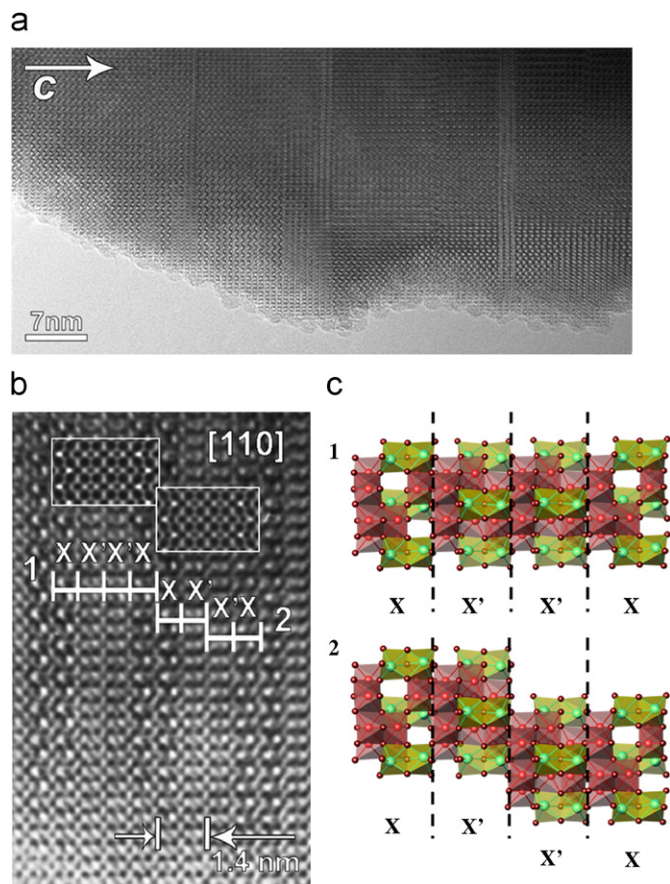
a

b

[110]

c

1

X | X' | X' | X

2

X | X'

X' | X

Fig. 10. (a) Low magnification showing defects interfaces and bands in $MgNi_3Nb_2O_9$; (b) [110] HREM image of $MgNi_3Nb_2O_9$. The simulations for defocus of −40 nm, thickness of 4 nm are outlined; (c) schematic representation.

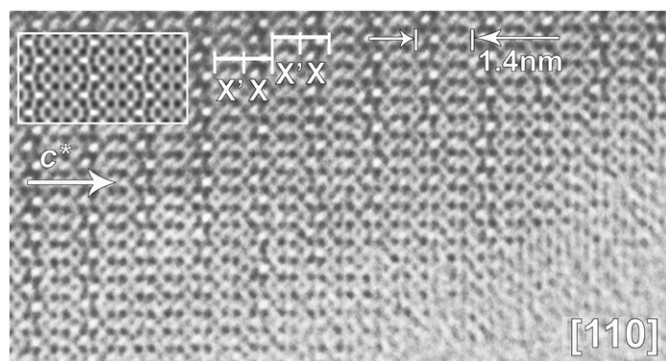Fig. 11. [110] HREM image of $MgNi_3Nb_2O_9$. The simulation for defocus of −40 nm, thickness of 40 nm is indicated by a white border.

3.2. Magnetic properties of $Mg_3NiNb_2O_9$ and $MgNi_3Nb_2O_9$

The magnetic susceptibility of the samples $Mg_3NiNb_2O_9$ and $MgNi_3Nb_2O_9$ has been measured after cooling in a zero field (ZFC) and in a field of 100 and 1000 Oe (FC), respectively. For the $Mg_3NiNb_2O_9$ curves—$\chi_{mol}(T)$, obtained in a zero magnetic field and a magnetic field of 100 Oe overlap, showing the absence of ferromagnetic
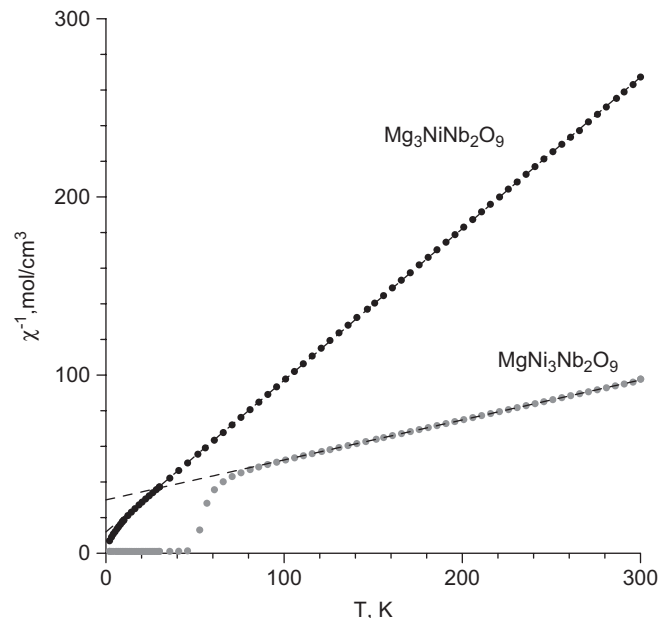

Fig. 12. Temperature dependence of inverse the magnetic susceptibility of $Mg_3NiNb_2O_9$ and $MgNi_3Nb_2O_9$ after cooling in a zero field and in a field 100 Oe.

ordering. It is shown that the temperature dependence of the magnetic susceptibility of the given phase obeys the Curie–Weiss law: $\chi = A_0 + C/(T-\Theta)$, where A_0 is the temperature-independent component of a magnetic susceptibility including diamagnetism, C is the Curie constant, Θ is the Weiss constant. From our experiments the following values were obtained: $A_0 = 4.930 \times 10^{-5}\,cm^3/mol$, $C = 1.159\,cm^3\,K/mol$, $\Theta = -13.1\,K$. The magnetic moment for Ni^{2+} is $3.04\,\mu_B$; this is slightly higher than the theoretical spin only value ($2.83\,\mu_B$). A slight deviation from linearity on a curve $1/\chi_{mol}(T)$, has been observed at temperatures below ~15 K (Fig. 12), which could be the evidence of a weak interaction between the paramagnetic centers. The susceptibility of $MgNi_3Nb_2O_9$ also follows the Curie–Weiss law ($A_0 = 9.270 \times 10^{-5}\,cm^3/mol$, $C = 4.522\,cm^3\,K/mol$, $\Theta = -137.2\,K$), but only above 150 K (Fig. 13). The magnetic moment at the Ni^{2+} ion in $MgNi_3Nb_2O_9$ is noticeably higher than in $Mg_3NiNb_2O_9$ and is equal to $3.45\,\mu_B$. A similar value of the magnetic moment, $3.54\,\mu_B$, is found in [16] for II-$Ni_4Nb_2O_9$. It is known that the effective reduction of the orbital part of the magnetic moment is typical for the $t_{2g}^6 e_g^2$ state. However, the value of the moment of the octahedral complex could be noticeably higher than the values of the spin only magnetic moments, because of the overlap with the multiplet excited state in which the spin–orbital coupling plays an essential role. The less the electronic levels are split by the crystal field, the higher the value of the magnetic moment. The influence of the excited states can be taken into account using effective g-factors $g = 2(1-\lambda/Dq)$ in the spin magnetic moment calculation $\mu^2 = g^2S(S+1)$, where λ is the constant of the spin–orbital interactions, Dq is the splitting in a crystal field [17]. A typical value of the constant of the spin–orbital
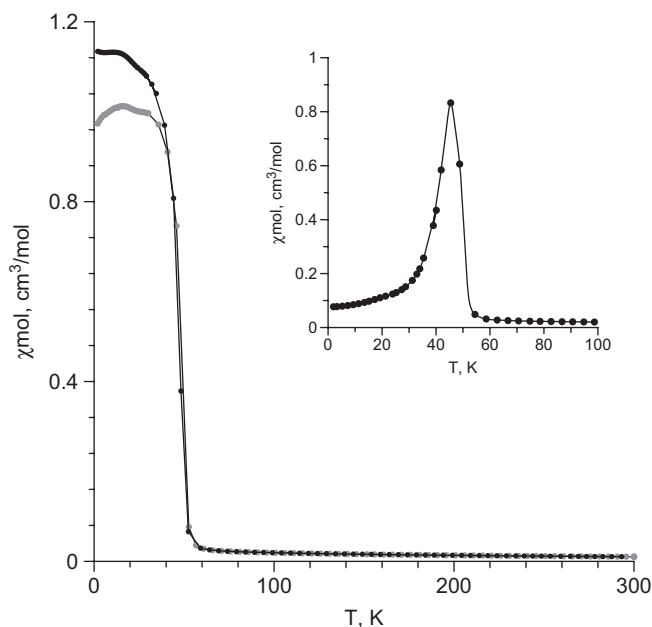
Fig. 13. Temperature dependence of the magnetic susceptibility of $MgNi_3Nb_2O_9$ after cooling in a field 1000 Oe (black) and in a zero field (grey). Inset: Temperature dependence of the *ac* susceptibility of $MgNi_3Nb_2O_9$.

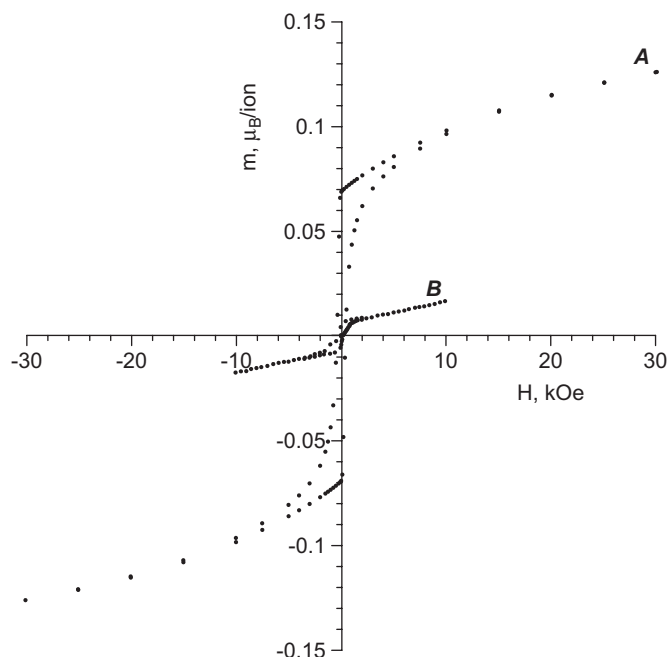Fig. 14. The magnetization as a function of the applied magnetic field for the ferrimagnetic phase $MgNi_3Nb_2O_9$ (A) and $Ni_4Nb_2O_9$ (B), measured at 2 K.

interactions for the ion Ni^{2+} is $350\,cm^{-1}$ [17], hence Dq for $Mg_3NiNb_2O_9$ and $MgNi_3Nb_2O_9$ are ~5000 and $\sim1600\,cm^{-1}$, respectively. Thus, differences in the value of the magnetic moments for the Ni^{2+} ions in $Mg_3NiNb_2O_9$ and $MgNi_3Nb_2O_9$ can be explained by the structural features of these niobates.

For $MgNi_3Nb_2O_9$ at temperatures below 50 K a divergence in the $\chi_{mol}(T)$ curves measured after cooling in a ZFC and in the field 1000 Oe has been observed, which is evidence of magnetic ordering (Fig. 13). The temperature dependence of the *ac* susceptibility (Fig. 13) shows a peak at 45.5 K. The decrease of the ferrimagnetic ordering temperature by a factor of ~1.7 in comparison with $Ni_4Nb_2O_9$ ($T_c = 76.1$ K [16]) is evidence of a diamagnetic dilution. Modules of the Weiss constants for these compounds have a difference of a factor ~1.6 ($\Theta_{Ni_4Nb_2O_9} = -215$ K [16]). These values correlate well with the number of bonds between nickel ions in $MgNi_3Nb_2O_9$ and $Ni_4Nb_2O_9$, which also have a 1.75 time difference. The magnetization curve as a function of the applied magnetic field for the ferrimagnetic phase of $MgNi_3Nb_2O_9$, measured at 2 K is shown in Fig. 14 as curve A. A similar hysteresis loop for $Ni_4Nb_2O_9$ [16] is shown in the same figure (curve B). The spontaneous magnetization and coercivity at $T = 2$ K for $MgNi_3Nb_2O_9$ are $0.06\,\mu_B$/ion and 400 Oe, respectively.

4. Conclusions

The possibility of obtaining solid solutions based on the II-$Ni_4Nb_2O_9$ structure has been shown. The boundaries of the solid solution $Mg_{4-x}Ni_xNb_2O_9$ ($0 \leqslant x \leqslant 2.75$) based on

the $Mg_4Nb_2O_9$ structure (space groups $P\bar{3}c1$) and the solid solution $Mg_{4-x}Ni_xNb_2O_9$ ($2.75 < x \leqslant 4$) based on the II-$Ni_4Nb_2O_9$ structure (space group $Pbcn$) have been determined experimentally. Transmission electron microscopy confirmed the data obtained from neutron powder diffraction; however several crystals of $MgNi_3Nb_2O_9$ showed planar imperfections that could be related to different kinds of ordering between the honey comb and the chain corundum layers. The extent and frequency of these defects suggest the possibility to obtain new modifications of corundum-related compounds. The influence of structural defects on the magnetic and microwave properties of $MgNi_3Nb_2O_9$ are not yet clear, however probably it will increase the microwave losses. Also, the appearance of uncompensated ferrimagnetism justifies the hope that the external magnetic field could be used as a force for the control and modeling of magnetic fields passing through the sample.

References

[1] M. Martin-Gonzalez, E. Moran, O.R. Fuente, M.A. Alario-Franco, J. Mater. Chem. 11 (2001) 616.
[2] S-Y. Cho, I.-T. Kim, K.S. Hong, J. Mater. Res. 14 (1999) 114.
[3] R. Guo, A.S. Bhall, J. Sheen, F.W. Ainger, S. Erdei, E.C. Sabbarao, L.E. Cross, J. Mater. Res. 10 (1995) 18.

[4] N.M. Alford, S.J. Penn, A. Templeton, X.J. Wang, J. Supercond. Sci. 10 (1997) 467.

[5] H. Ogawa, A. Kan, S. Ishihara, Y. Higashida, J. Eur. Ceram. Soc. 23 (2003) 2485.

[6] A. Kan, H. Ogawa, H. Ohsato, J. Ceram. Soc. Jpn. 112 (2004) 1622.

[7] A. Kan, H. Ogawa, A. Yokoi, H. Ohsato, Jpn. J. Appl. Phys. 42 (2003) 6154.

[8] A. Yokoi, H. Ogawa, A. Kan, H. Ohsato, Y. Higashida, J. Eur. Ceram. Soc. 25 (2005) 2871.

[9] A. Kan, H. Ogawa, A. Yokoi, Y. Nakamura, J. Eur. Ceram. Soc. 27 (2007) 2977.

[10] A. Yoshida, H. Ogawa, A. Kan, S. Ishihara, Y. Higashida, J. Eur. Ceram. Soc. 24 (2004) 1765.

[11] R.J. Cava, J. Mater. Chem. 11 (2001) 54.

[12] R. Wichmann, Hk. Muller-Buschbaum, Z. Anorg. Allg. Chem. 539 (1986) 203.

[13] A.C. Larson, R.B. Von Dreele, "GSAS" LANSCE, MS-H805. Los Alamos National Laboratory, Los Alamos, NM 87545.

[14] N. Kumada, K. Taki, N. Kinomura, Mater. Res. Bull. 35 (2000) 1017.

[15] R. Wichmann, Hk. Muller-Buschbaum, Z. Anorg. Allg. Chem. 525 (1985) 135.

[16] H. Ehrenberg, G. Wltschek, H. Weitzel, F. Trouw, J.H. Buettner, T. Kroener, H. Fuess, Phys. Rev. B 52 (1995) 9595.

[17] B.R. McGarvey, Transit. Metal Chem. 3 (1966) 90.